Supporting Information:

Phase-Resolved Detection of Ultrabroadband THz Pulses inside a Scanning Tunneling Microscope Junction

Melanie Müller[1]*, Natalia Martín Sabanés[1,2], Tobias Kampfrath[1,2], and Martin Wolf[1]

[1]*Department of Physical Chemistry, Fritz Haber Institute of the Max Planck Society, Faradayweg 4-6, 14195 Berlin, Germany.*

[2]*Department of Physics, Freie Universität Berlin, Arnimallee 14, 14195 Berlin, Germany.*

*Corresponding author: m.mueller@fhi-berlin.mpg.de

10 pages, 5 figures

1. **Discussion of space charge effects**
2. **Dependence of THz waveforms on DC bias and THz voltage**
3. **Antenna model**
4. **Measurement of incident THz electric fields**
5. **Dependence of THz spectra and amplitude on STE position**
6. **Estimation of tip-sample distance at the set point**
7. **Numerical simulation of THz electromagnetic field distributions**

1. Discussion of space charge effects

Sampling the THz voltage across the STM junction via THz-induced modulation of the photocurrent requires that the photocurrent reacts quasi-instantaneous on the time scale of the applied THz field. However, several effects such as photoelectron propagation in the tip-sample gap or long-lived hot carriers in the photoexcited tip or sample may disturb the measurement and have to be ruled out. As discussed by Yoshida et al.,[1] THz-Streaking back into the tip can be circumvented by operating at high DC bias and low THz fields[a], whereas lifetime effects from hot carriers can be neglected when operating in the regime of multiphoton photoemission above the potential barrier. Another effect, not considered by Yoshida et al.,[1] is space charge, that is, the Coulomb repulsion experienced by electrons in a photoelectron cloud containing multiple electrons. Due to the nanometer-sized volume at the tip apex, even a low number of electrons can lead to high photoelectron densities, leading to strong Coulomb interaction between the photoelectrons. As a consequence, 'leading' photoelectrons at the front of the space charge cloud are accelerated away from the tip faster than by the DC acceleration alone, whereas 'backside' photoelectrons close to the tip surface are accelerated back towards the tip by the space charge cloud in front of them. Those back-accelerated electrons can then be steered back into the tip by THz fields much lower than the DC field due to the described effect of space charge acceleration. Moreover, these photoelectrons are not rapidly accelerated away from the tip as expected from the large inhomogeneous DC field at the tip, but can remain a significant amount of time close to the tip surface. Hence, they not only experience the instantaneous THz field at the time of photoemission, but can be steered back into the tip by a THz field at a much later delay within the THz pulse, i.e., the overall process is not instantaneous and can act as an effective low pass filter distorting the measured THz waveform.

In Figure S1 we plot THz waveforms measured in the STM junction at 1 µm gap distance and 8 V DC bias for different photocurrents. The applied THz voltage is 0.12 V at the maximum peak. As can be seen from Figure S1a), the measured waveform clearly depends on the number of electrons excited per laser pulse, with a most pronounced deformation at the beginning of

[a] It should be noted that, even at low THz and high DC fields, the THz field always affects the photoelectron trajectories in the tip-sample gap, depending on the emission time and flight time of the photoelectrons with respect to the arrival and duration of the THz pulse. As we detect the total current and average over all energies and arrival times of the photoelectrons, our measurement is not sensitive to small modulations of the electron trajectories, but is only sensitive to a reduction of the total electron yield by THz-streaking back into the tip.

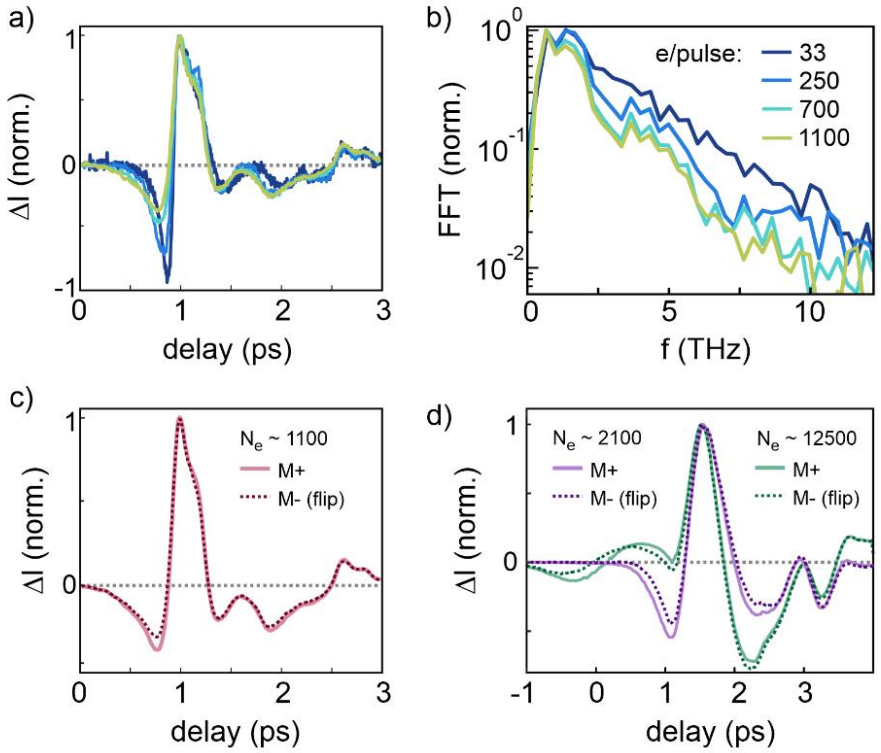

Figure S1. (a) Tip-enhanced THz waveforms and (b) corresponding Fourier amplitude spectra measured in the STM junction for increasing numbers of photoelectrons emitted per NIR pulse (corresponding increasing pulse energies $E_{p,STM}$ are 0.45 nJ, 0.95 nJ, 1.42 nJ and 1.8 nJ). Large electron numbers/densities lead to low-pass filtering presumably due to space charge. In the presence of space charge, the THz waveforms for opposite THz polarities exhibit different shapes, as shown in (c) for 1100 e/pulse ($E_{p,STM} = 1.8$ nJ) and (d) for 2100 e/pulse ($E_{p,STM} = 4$ nJ) and 12500 e/pulse ($E_{p,STM} = 12.5$ nJ). At very high electron density, severe waveform distortions occur. We note that (d) has been measured for a different tungsten tip. ($d = 1$ µm, $U_{DC} = 8$ V, $E_{p,STE} = 0.4$ µJ, $U_{THz,peak} = 0.12$ V)

the pulse before the main half cycle. This is accompanied by a reduction of the THz bandwidth as plotted in Figure S1b), revealing the effective low pass filtering due to space charge. Moreover, Figure S1c) shows that in this regime the shape of the THz waveform also depends on the THz polarity. These deformations and deviations with polarity are most pronounced at the beginning of the THz pulse. This is not surprising as those photoelectrons excited shortly before the arrival of the main pulse experience the strongest THz field, whereas the photoelectrons excited at later times only experience the ringing oscillations after the main THz cycle. For even higher electron numbers, severe waveform distortions are observed as plotted in Figure S1d), with distortions and polarity dependence occurring over the full THz waveform. Understanding the exact waveform deformations in the presence of space charge requires a detailed analysis of the dynamics of the photoelectron cloud in the tip-sample gap and is beyond the scope of this work. At this point, we conclude that elimination of space charge contributions is crucial for reliable THz waveform sampling by the employed technique as described in the

main manuscript. In our experiments we proof the absence of space charge effects to our measurements by systematically reducing the number of photoelectrons to a value at which no waveform distortions and no spectral filtering is observed by further lowering the photocurrent. These observations point out the importance for a careful consideration of non-instantaneous effects potentially disturbing the sampled THz voltage transient.

2. Dependence of THz waveforms on DC bias and THz voltage

The propagation of photoelectrons in the tip-sample gap (and potentially back to the tip) depends on the combined forces of the DC field, the THz field, and space charge interactions. Moreover, waveform distortions from photoassisted tunneling of electrons close to the Fermi level with longer lifetimes may be expected to contribute at high DC bias and short gap distances. As the lifetime of hot electrons depends on the energy window sampled by the THz pulse, distorting effects from hot carriers should also depend on the DC bias and THz voltage amplitude. Hence, undistorted instantaneous THz near-field sampling requires that the measured THz waveform does not depend on the DC bias and incident THz field strength within the linear range of the I_{Ph}-V slope (see Figure 1c)). Figure S2b) shows THz waveforms measured for three different DC biases with the corresponding I_{Ph}-V curve plotted in Figure S2a). All waveforms exhibit the same shape and voltage amplitude as expected from the linear slope of the I-V curve. Figure S2c) shows THz waveforms measured for two incident THz amplitudes at 10 V bias, and again we find that the sampled THz waveform does not depend on the applied THz voltage. In addition to the constant THz waveform observed for opposite THz polarities, as plotted in Figure 1d) in the main manuscript, these results confirm the interpretation and validity of our sampling approach.

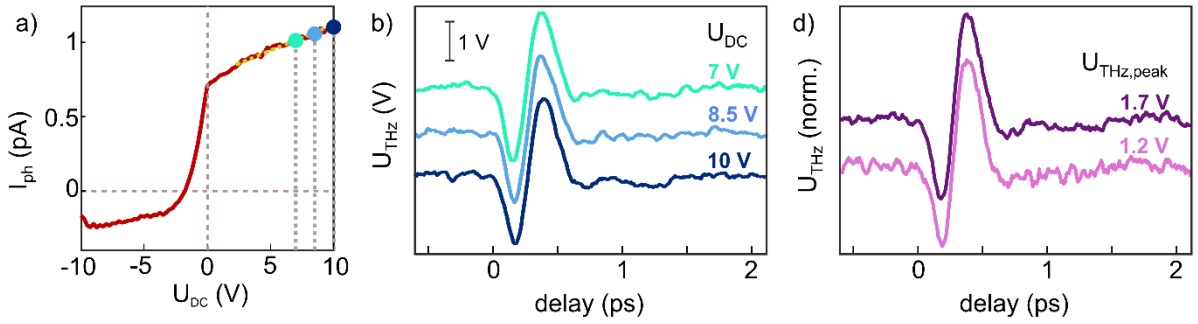

Figure S2. (a) I-V curve used for calibration of the tip-enhanced THz waveforms shown in (b) and (c). THz waveforms are measured in the STM at (b) different DC biases ($E_{p,STE} = 0.9$ µJ, $U_{THz,peak} = 1.9$ V) and (c) different THz amplitudes ($U_{DC} = 10$ V, $E_{p,STE} = 0.48$ µJ and $E_{p,STE} = 0.9$ µJ) in the linear part of the I-V slope. ($d = 1$ µm, STE position $\Delta z_{STE} = -2.6$ mm). These data were measured with a Ag-tip sharpened by a focused ion beam milling. Similar results are obtained from tungsten and Pt/Ir tips.

3. Antenna model

The model used to fit the tip antenna response in Figure 2 treats the tip as an *RLC* electronic circuit with resistance *R*, capacitance *C* and inductance *L* connected in series. In this very simple model, the incident THz electric field applies a voltage to the antenna that leads to a current induced inside the antenna of

$$I_{\mathrm{THz}}(\omega) \propto \frac{E_{\mathrm{in}}(\omega)}{R + i\omega L - i(\omega C)^{-1}} \ .$$

Best reproduction of the THz voltage transient from the incident THz waveform is obtained for circuit parameters of $R = 300\ \Omega$, $L = 0.32$ nH and $C = 35$ fF, indicating an effective antenna length of ~1 mm for a 300 µm thick wire. These values are in good agreement with previously reported results[2,3]. The simple *RLC* model considers only the tip wire alone as the antenna. A more detailed theoretical analysis of the receiving properties of an STM junction requires more advanced models taking into account the dielectric response of the sample, the exact STM environment, and scattering e.g. at the tip shaft or at the tip mount.

4. Measurement of incident THz electric fields

To analyze the THz electric field incident to the STM junction, we pick the THz beam before entering the STM chamber and focus the THz pulses in a 300 µm thick ZnTe(110) crystal for electro-optic sampling. The path length and optical components are identical to the STM beam path. In EOS, the measured time-domain signal $S(t)$ is given by the convolution of the THz electric field $E_{\mathrm{in}}(t)$ incident on the detector with the detector response function h_{det},

$$S(t) = (h_{\mathrm{det}} * E_{\mathrm{in}})(t).$$

Hence, if $h_{\mathrm{det}}(t)$ is known, the THz electric field can be obtained by deconvolution of the EOS signal with the detector response, which depends on the properties and thickness of the electro-optic medium and the sampling pulses. After calculation of $h_{\mathrm{det}}(t)$, the deconvolution is performed numerically as described in more detail in references[4,5]. Figure S3a) shows the deconvoluted waveforms of the THz electric field incident on the STM tip for the four STE positions plotted in Figure 3b). As mentioned in the manuscript, the measured EOS amplitude at frequencies >5 THz is comparably low, leading to increased noise at higher frequencies in the broadband deconvolution process. This can be mitigated by using thinner detection crystals. However, echos in the first picoseconds caused by reflections inside the detection crystal can complicate the analysis of the transfer function in this case.

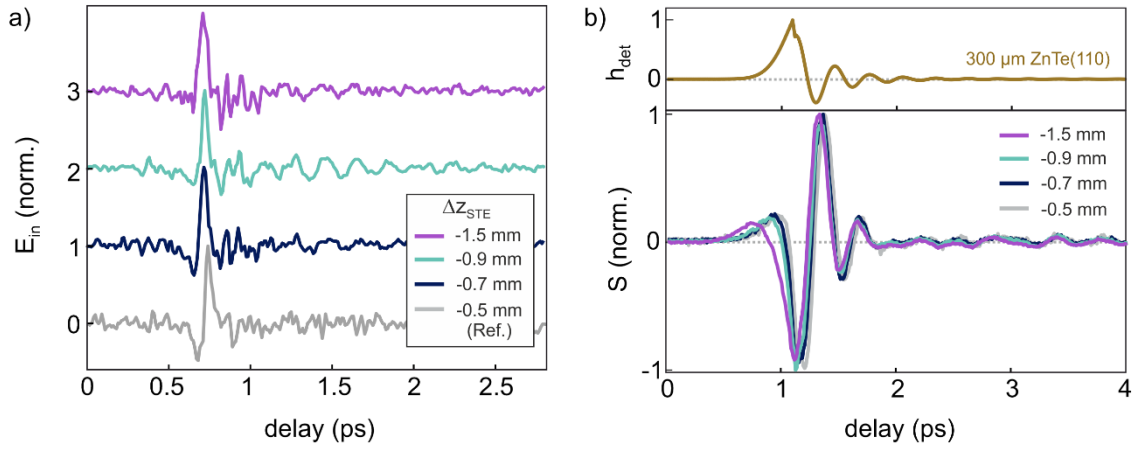

Figure S3. (a) THz electric field transients incident onto the ZnTe(110) detection crystal for four different STE positions as obtained from deconvolution of the EOS signal with the detector response. The phase shift applied by moving the STE inside the focused NIR beam is apparent in the waveforms. (b) Corresponding EOS signals (bottom) and detector response function $h_{det}(t)$ (top).

Direct comparison of the THz electric field obtained from EOS and the THz voltage waveform measured in the STM requires that both waveforms are recorded at the same position along the focused THz beam. In the EOS setup, the detection crystal is positioned in the focus of the tightly focused NIR beam that propagates collinear with the THz beam and is used as sampling pulse. Likewise, we use the same collinearly propagating NIR pulses as alignment beam to adjust the THz focus on the tip in the STM. Precise alignment is hereby ensured by monitoring the light reflected off the Ag sample and collected via the second (Ag) parabolic mirror inside the STM chamber, and by optimization of NIR-induced photoemission from the tip apex.

5. Dependence of THz spectra and amplitude on STE position

As discussed in the main manuscript, the THz spectra can vary slightly with STE position. Figures S4a) and S4b) show the THz amplitude spectra of the tip-enhanced THz waveforms plotted in Figures 3b) and 4b), respectively. We observe a slight bandwidth reduction upon moving the STE away from the NIR focus. We assign such variation of the THz spectrum to the imperfect imaging of the THz focus onto the tip at STE positions outside the NIR focal plane. The variation of the peak THz voltage amplitude with STE position Δz_{STE} is shown in Figure S4c). Maximizing simultaneously the THz amplitude and bandwidth requires a modified STE geometry optimized for our laser parameters, which is currently under investigation.

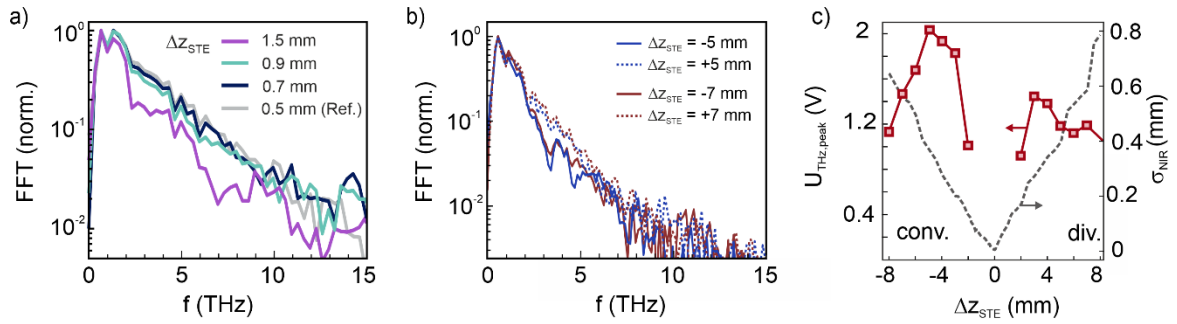

Figure S4. Fourier amplitude spectra of the tip-enhanced THz waveforms vs STE position shown (a) in Figure 3b), and (b) in Figure 4b). We observe a red-shift of the spectra and slightly reduced THz bandwidth when moving the STE away from the focus. (c) Peak THz voltage as a function of STE position ($E_{p,STE}$ = 1.2-μJ). The black dashed line shows the NIR pump spot size vs STE position (right y-axis).

6. Estimation of tip-sample distance at the set point

The actual tip-sample distance under NIR illumination is estimated as follows: First, we estimate the change in gap distance due to removal of the photoinduced current contribution by measuring the prompt (~30 ms, which is the time required to reach again the set point current) reduction in gap distance upon blocking the NIR beam, which gives $\Delta d_{\mathrm{ph}} \cong 1.6$ nm. Second, we estimate the absolute distance of the 'dark' junction by measuring the z-dependence after thermal equilibration and extrapolation of the *I*-*z*-curve to the quantum conductance G_0. This yields a tip-sample distance of $\Delta d_{\mathrm{DC}} \cong 3$ nm at 8 V without illumination. We obtain the same distance Δd_{DC} by extrapolating *I*-*z*-curves at 1 V set bias (yielding 1 nm gap distance) and observation of the change of the z-piezo position by manually changing the set bias from 1 V to 8 V during feedback (which gives ~2 nm). The absolute distance of the illuminated junction is then estimated to be the sum of the two contributions, $d = \Delta d_{\mathrm{DC}} + \Delta d_{\mathrm{ph}} = 4.6$ nm. Although this procedure neglects possible influences of the tip temperature on the DC current, it gives a reasonable estimate of the actual tip-sample distance.

7. Numerical simulation of THz electromagnetic field distributions

Numerical simulations are performed to calculate the THz response of the STM tip by solving the time-harmonic wave equation for the electric field within the RF-Module of COMSOL Multiphysics 5.5. For a given excitation frequency, COMSOL solves for the full time-harmonic electromagnetic field distribution. Static field distributions are calculated using the AC/DC module of COMSOL. Simulations are performed in 3D with the tip oriented along the z-axis. The tip is modelled by a conical wire with a half opening angle of 4° terminating in an apex of 50 nm radius. The sample of 10 μm thickness is placed at a variable distance *d* in front of the

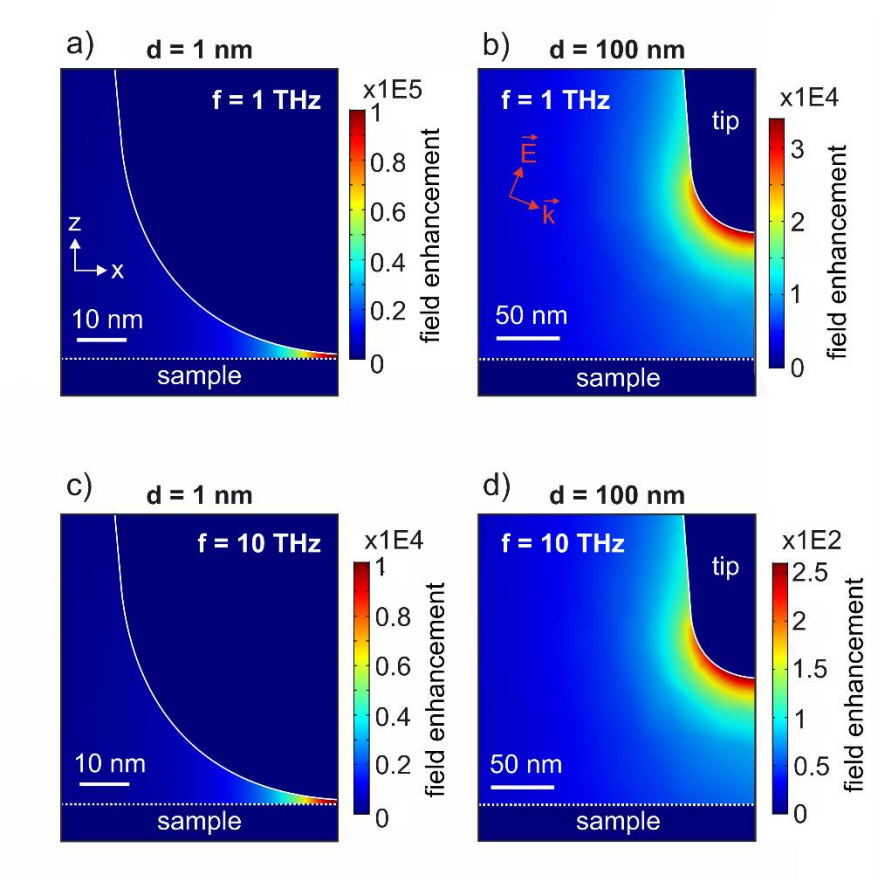

Figure S5. Spatial distributions of the tip-enhanced THz electric field (normalized field) in the tip-sample junction at 1 nm and 100 nm gap distances for frequencies of (a-b) 1 THz and (c-d) 10 THz, respectively. The color bars represent the enhancement of the THz field inside the junction with respect to the incident THz field amplitude. The red arrows indicate the direction and polarization of the incident THz field. Simulation parameters are described in the text.

tip. The width of the simulation volume is 200×200 µm and the wire is truncated by the end of the simulation volume at a height of 200 µm from the apex. The simulation volume is surrounded by perfectly matched layers to absorb all outgoing waves. The tip-sample junction is illuminated by plane-wave THz radiation propagation along the x-direction at an angle of 68° with respect to the tip axis as and is polarized linearly in the x-z-plane, as indicated by the red arrows in Figure S5b). The simulation volume is cut in half along the y-direction (out of plane) according to the symmetry given by the THz beam direction to reduce the computational cost. The materials properties of the tip and sample are determined from the complex dielectric functions of tungsten and silver, whose real and imaginary parts are calculated from the Lorentz Drude model with the Lorentz-Drude parameters taken from Rakic et al.[6].

Figures S5a)-d) show spatial distributions of the tip-enhanced THz electric field in the tip-sample junction for two THz frequencies. As can be seen from the color scales, the THz field enhancement increases significantly with lower THz frequencies and shorter gap distances. At

far distances b) and d), the strongly inhomogeneous THz near-field is confined to the tip apex with a spatial extent given by the tip radius, and decays rapidly with larger distances away from the tip surface. At nanometer distances much smaller than the tip radius, the field becomes spatially more localized inside the tip-sample gap, and becomes homogeneous like in a plate-capacitor at the junction center $(x, y) = (0,0)$. We obtain the THz-field-induced potential difference from the computed fields by line integration of the z-component of the THz near-field along the center of the junction at $(x, y) = (0,0)$. We confirmed that line integration along other pathways yields the same THz-induced potential difference.

References

(1) Yoshida, S.; Hirori, H.; Tachizaki, T.; Yoshioka, K.; Arashida, Y.; Wang, Z. H.; Sanari, Y.; Takeuchi, O.; Kanemitsu, Y.; Shigekawa, H. Subcycle Transient Scanning Tunneling Spectroscopy with Visualization of Enhanced Terahertz Near Field. *ACS Photonics* **2019**, *6* (6), 1356–1364. https://doi.org/10.1021/acsphotonics.9b00266.

(2) Wimmer, L.; Herink, G.; Solli, D. R.; Yalunin, S. V.; Echternkamp, K. E.; Ropers, C. Terahertz Control of Nanotip Photoemission. *Nat. Phys.* **2014**, *10* (May), 432–436. https://doi.org/10.1038/nphys2974.

(3) Wang, K.; Mittleman, D. M.; Van Der Valk, N. C. J.; Planken, P. C. M. Antenna Effects in Terahertz Apertureless Near-Field Optical Microscopy. *Appl. Phys. Lett.* **2004**, *85* (14), 2715–2717. https://doi.org/10.1063/1.1797554.

(4) Seifert, T.; Jaiswal, S.; Martens, U.; Hannegan, J.; Braun, L.; Maldonado, P.; Freimuth, F.; Kronenberg, A.; Henrizi, J.; Radu, I.; et al. Efficient Metallic Spintronic Emitters of Ultrabroadband Terahertz Radiation. *Nat. Photonics* **2016**, *10* (7), 483–488. https://doi.org/10.1038/nphoton.2016.91.

(5) Seifert, T. S.; Jaiswal, S.; Barker, J.; Weber, S. T.; Razdolski, I.; Cramer, J.; Gueckstock, O.; Maehrlein, S. F.; Nadvornik, L.; Watanabe, S.; et al. Femtosecond Formation Dynamics of the Spin Seebeck Effect Revealed by Terahertz Spectroscopy. *Nat. Commun.* **2018**, *9* (1), 1–11. https://doi.org/10.1038/s41467-018-05135-2.

(6) Rakic, A. D.; Djurišic, A. B.; Elazar, J. M.; Majewski, M. L. Optical Properties of Metallic Films for Vertical-Cavity Optoelectronic Devices. *Appl. Opt.* **1998**, *37* (22), 5271. https://doi.org/10.1364/AO.37.005271.